
CAUSAL COUPLING INFERENCE FROM MULTIVARIATE TIME SERIES BASED ON ORDINAL PARTITION TRANSITION NETWORKS

Narayan Puthanmadam Subramaniyam
Faculty of Medicine and Health Technology
Tampere University
narayan.subramaniyam@tuni.fi

Reik V. Donner
Magdeburg–Stendal University of Applied Sciences
Potsdam Institute for Climate Impact Research

Davide Caron
Enhanced Regenerative Medicine
Istituto Italiano di Tecnologia

Gabriella Pannucio
Enhanced Regenerative Medicine
Istituto Italiano di Tecnologia

Jari Hyttinen
Faculty of Medicine and Health Technology
Tampere University

May 28, 2022

ABSTRACT

Identifying causal relationships is a challenging yet a crucial problem in many fields of science like epidemiology, climatology, ecology, genomics, economics and neuroscience, to mention only a few. Recent studies have demonstrated that ordinal partition transition networks (OPTNs) allow to infer the coupling direction between two dynamical systems. In this work, we generalize this concept to the interaction between multiple dynamical systems and propose a new method to detect causality in multivariate observational data. We demonstrate that our approach can reliably identify the direction of interaction and the corresponding delays with numerical simulations using linear stochastic systems as well as nonlinear dynamical systems such as a network of neural mass models. Finally, we apply our method to real-world observational microelectrode array data from rodent brain slices to study the causal effect networks underlying epileptic activity. Our results from simulations as well as real-world data suggest that OPTNs can provide a complementary approach to reliably infer causal effect networks from multivariate observational data.

Keywords Causality · Transition networks · Information theory · Time series analysis

1 Introduction

The detection of causal interactions is one of the fundamental problems in both natural and social sciences [1,2]. Reliable inference of causality can aid in making predictions that may eventually allow to design intervention strategies [3]. For example, in neurological disorders such as epilepsy, predicting a seizure and preventing its occurrence is one of the long-standing unsolved problems. In fact, seizure prediction algorithms and consequent effective interventions to prevent seizure occurrence could be life-saving for the patient.

In the past few decades, several approaches have been developed to both identify and quantify the interdependence between multiple time series. The Granger causality (GC) test can be used to infer causality between two time series [4], and its extension of partial directed coherence (PDC) allows to infer causality from multivariate data [5]. The general idea behind GC is based on linear regression. Under this framework, a causal relation from one system (or variable) X to another system Y (i.e., $X \rightarrow Y$) is inferred if the variance of the prediction error of the signal of Y can be reduced by including past information about the signal X in the regression model. Since classical GC analysis is model

based and only valid for linear systems, bivariate causality measures based on information theory have been proposed for a corresponding application to non-linear systems [6]. These methods include, among others, transfer entropy (TE) [7], time-delayed mutual information [8] and the multivariate extension of TE (MTE) [6]. In particular, TE can be considered as a generalization of GC for nonlinear systems [9], while it has been shown to be equivalent to GC for linear Gaussian models [10].

Recently there has been a lot of interest in characterizing dynamical systems using network based time series analysis methods [11]. Such analysis methods include, among others, recurrence networks [12–14], visibility graphs [15] and transition networks [16], all of which feature different definitions of nodes and links of network representations of the time series. For instance, in the case of recurrence networks, the edges are defined based on the proximity of observation vectors in phase space, whereas for visibility graphs [12] mutually visible elements in a time series are linked to form a network [15]. Finally, in the case of transition networks [16], certain discrete states or patterns are defined as nodes, and if one of these dynamical structures is followed by the other with nonzero probability along the observed (or reconstructed) trajectory, a directed edge is established between the corresponding nodes [17]. However, the majority of the aforementioned methods have focused on univariate time series, while the generalization to multivariate time series as necessary to detect signatures of causality has not yet been systematically explored in full detail.

In this work, we use a particular class of transition networks known as ordinal partition transition networks (OPTNs) [18] to infer causality from multivariate time series. OPTNs are based on identifying ordinal patterns in time series, originally proposed in [19], reflecting the respective rank order among a sequence of univariate observation values. This results in a specific symbolic representation of the observed system’s trajectory based on a univariate time series. With this symbolic encoding, we define an OPTN that consists of nodes representing ordinal patterns and probability weighted edges that represent the transition frequencies between two successive ordinal patterns [17]. It has been shown that the ordinal partition has the generating property under specific conditions, which makes it attractive as it implies topological conjugacy between phase space and the ordinal symbolic dynamics [16]. Furthermore, given the symbolic representation of the phase space trajectory (which controls the respective frequency of the different ordinal patterns), it is possible to compute a variety of dynamical characteristics such as permutation entropy or a plethora of possible complexity measures. For an unconstrained stochastic process, all possible ordinal patterns occur with equal probability, whereas for a time series produced by deterministic dynamics, certain ordinal patterns commonly do not appear; these are known as forbidden patterns [20]. Previous applications of complexity measures derived from OPTNs include the classification of cardiac dynamics using electrocardiography data [16,21] and analysis of electroencephalography (EEG) data from healthy and epileptic humans [22].

Although recent attempts have focused on bi- and multivariate extensions of OPTNs [20], with the aim of characterizing different types of synchronization transitions, they did not yet provide thorough information about causal relationships among multivariate data. Recently, Ruan *et al.* [17] proposed a strategy for the estimation of several complexity measures based upon bipartite OPTNs to infer the coupling direction between paired time series. However, their approach has been limited by the fact that it is bivariate in nature and thus, when applied to a multivariate data set, it cannot distinguish between direct and indirect causal connections among the individual signals. To overcome this limitation, in this work, we propose to extend OPTN based time series analysis to account for truly multivariate (more than two components) time series by constructing multipartite OPTNs. We also propose an approach to distinguish direct from indirect causal connections, based on conditional Shannon entropy [17]. We apply our method to two different artificial data sets that include coupled stochastic processes with linear and nonlinear interactions as well as data simulated with a population of coupled neural mass models (NMM), which are described by a set of ordinary differential equations, to mimic the dynamics exhibited by neurophysiological time series [23]. Finally, as a real world example, we consider *in vitro* microelectrode array (MEA) recordings from a rodent brain slice preparation in which epileptiform discharges are induced by pharmacological treatment.

2 Methodology

2.1 Ordinal partition transition networks

Given a univariate time series $X = \{x_t\}_{t=1}^T$, following Takens’ embedding theorem, we can reconstruct its phase space trajectory by using M successively lagged replications of X , each separated by a lag d , yielding the vector

$$\mathbf{z}_t = [x_t, x_{t+d}, \dots, x_{t+(M-1)d}], \quad (1)$$

for $t = 1$ to $T - (M - 1)d$, where M and d are the embedding dimension and delay, respectively. Each embedding vector \mathbf{z}_t is mapped to a sequence of integers $(s_0, s_1, \dots, s_{M-1})$ that describes the rank order of its components (with 0 indicating the smallest value) and is a unique permutation of the set $\{0, 1, \dots, M - 1\}$, thereby satisfying

$$x_{t+s_0d} \leq x_{t+s_1d} \leq x_{t+s_2d} \leq \dots \leq x_{t+s_{M-1}d} \quad (2)$$

and

$$s_{l-1} < s_l \quad \text{if} \quad x_{t-s_{l-1}} = x_{t-s_l} \quad (3)$$

Note that there exist $M!$ different possible ordinal patterns when a time series is embedded in M dimensions, and we denote these patterns by $\pi_1, \pi_2, \dots, \pi_{M!}$.

As an example, consider a 5-dimensional embedding of a time series yielding an embedding vector

$$\{x_t, x_{t+d}, x_{t+2d}, x_{t+3d}, x_{t+4d}\} = \{3, 9, 10, 1, 6\}. \quad (4)$$

Here, $x_{t+3d} < x_t < x_{t+4d} < x_{t+d} < x_{t+2d}$, and thus this partition would be mapped to the ordinal pattern or symbol $\pi_k = \{3, 0, 4, 1, 2\}$. The exact numerical value of the resulting integer index $k \in \{1, \dots, M!\}$ depends on the specific sorting of the permutations, the default of which may differ among different algorithms and programming language.

For a univariate time series, we can then construct an (unweighted or weighted) ordinal partition transition network (OPTN) with $M!$ nodes by first repeating this encoding procedure for each embedding vector. A weighted OPTN is obtained by setting the weight of the edge between two nodes (permutations) to be equal to the empirical frequency of ‘‘transitions’’ (i.e., successive occurrences) between the corresponding possible ordinal patterns. An unweighted OPTN simply contains a directed edge of unit weight between the corresponding nodes if this frequency is nonzero.

Ruan *et al.* extended the idea of OPTNs to bivariate time series, that may be interacting linearly or non-linearly [17]. In their framework, given the time series $\{x_{1,t}\}_{t=1}^T$ and $\{x_{2,t}\}_{t=1}^T$, derived from two dynamical systems X_1 and X_2 , we can derive the associated sequences of ordinal patterns underlying each time series as described above, containing the ordinal patterns $\pi_i^{x_1}$ and $\pi_j^{x_2}$ for X_1 and X_2 , respectively. One can now compute the (instantaneous or time-lagged) conditional co-occurrence frequencies $p(\pi_j^{x_2} | \pi_i^{x_1, \tau})$ by simply counting the number of cases in which $\pi_j^{x_2}$ occurs with a time-lag of τ following an occurrence of $\pi_i^{x_1}$. Note that that we deviate here from the notation in [17] in order to allow a straightforward generalization of the concept of co-occurrence probabilities by including multiple variables X_i that may possibly cause variations of the given X_2 at different delays τ_i (see Section 2.2 below). Thus, $\tau = 0$ corresponds to looking at simultaneous co-occurrence while $\tau > 0$ would imply looking at lagged co-occurrence. Given these conditional co-occurrence frequencies, Ruan *et al.* proposed the estimation of the conditional Shannon entropy [17], given as

$$H_\tau(X_2|X_1) = - \sum_{i=1}^{M!} \sum_{j=1}^{M!} p(\pi_i^{x_1, \tau}, \pi_j^{x_2}) \log_2 p(\pi_j^{x_2} | \pi_i^{x_1, \tau}), \quad (5)$$

which gives the interaction $X_1 \rightarrow X_2$ at a delay of τ . The interaction in the other direction at lag τ , $X_2 \rightarrow X_1$ can be defined in an analogous way as follows,

$$H_\tau(X_1|X_2) = - \sum_{i=1}^{M!} \sum_{j=1}^{M!} p(\pi_j^{x_2, \tau}, \pi_i^{x_1}) \log_2 p(\pi_i^{x_1} | \pi_j^{x_2, \tau}), \quad (6)$$

If X_1 and X_2 are independent and their different ordinal patterns uniformly distributed, then $p(\pi_j^{x_2, \tau}, \pi_i^{x_1}) = \frac{1}{(M!)^2}$ and $p(\pi_i^{x_1} | \pi_j^{x_2, \tau}) = \frac{1}{M!}$ and thus $H_\tau(X_1|X_2) = \log_2 M!$, which is the upper bound for the conditional entropy value, denoted as H_{max} . On the other hand, if X_1 and X_2 are fully dependent, then $p(\pi_i^{x_1} | \pi_j^{x_2, \tau}) = 1$ and ideally $H_\tau(X_1|X_2) = 0$. Thus, as the strength of causal interaction from X_2 to X_1 at a given time lag τ increases, $H_\tau(X_1|X_2)$ decreases.

2.2 Causal inference strategy based on entropy measures from OPTNs

When dealing with multivariate data, i.e. data from three or more interacting systems, it is necessary to distinguish direct links from indirect ones. For example, consider a transitive chain $X_1 \rightarrow X_2 \rightarrow X_3$ (Figure 1 (A)). Applying the bivariate OPTN derived entropy measure as described in [17] would lead to the detection of a non-existing connection from $X_1 \rightarrow X_3$, as shown in Figure 2 (A). Similarly, consider a fork pattern, where $X_1 \rightarrow X_2$ and $X_1 \rightarrow X_3$ (Figure

1 (B)). Here, X_1 is a common driver to both X_2 and X_3 and this will lead to a spurious connection between the X_2 and X_3 as shown in Figure 2 (B). Note that in Figure 2, an interaction $m \rightarrow n$ at negative delay is to be interpreted as $n \rightarrow m$.

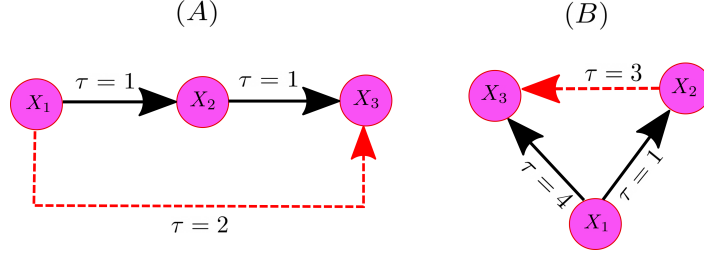


Figure 1: Example of spurious connections (shown as dotted red arrows) that would be inferred from a directed chain (A) and a fork pattern (B) if direct links are not distinguished from indirect links.

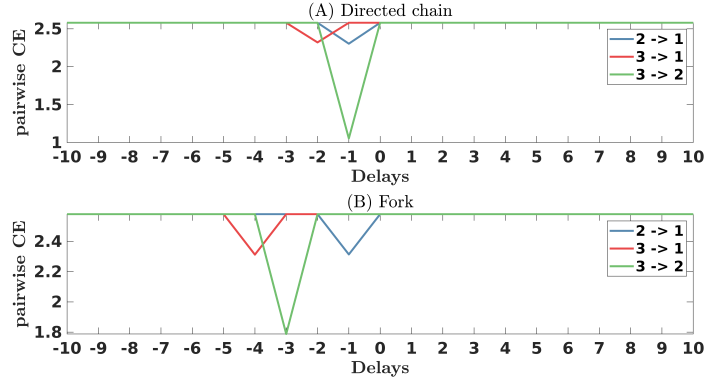


Figure 2: Causal network inferred with the bivariate approach using OPTN based conditional co-occurrence entropy for the directed chain (A) and fork (B) with a spurious connection $1 \rightarrow 2$ at $\tau = 2$ for the directed chain and $2 \rightarrow 3$ at $\tau = 3$ for the fork pattern.

In order to distinguish such direct from indirect links, a sophisticated way of conditioning has to be employed, thereby generalizing the previous strictly bivariate approach. In the following, we will detail a possible methodology to use OPTN based entropy measures to infer causality from multivariate time series as outlined in Figure 3. Note that this methodology rests upon certain general assumptions common to causal inference methods, most notably, the completeness of the set of variables analyzed (i.e. the absence of any possible hidden drivers).

STEP I : Pre-processing of observational data

Depending on the particular research problem, observational time series first have to be pre-processed, which includes standard procedures like band-pass filtering, resampling and removal of any noise or artifacts if present. If necessary, the data can be further divided into a number of overlapping windows to obtain a time-dependent estimate of the coupling measure (see below).

STEP II : Construction of multiple OPTNs

Given a time series, its phase space is reconstructed following Takens’ embedding theorem. The components of the resulting embedding vectors are then rank ordered to obtain the symbolic representation of the time series. For an N -channel multivariate time series, N such OPTNs are constructed, which will be referred to as multiple OPTNs (M-OPTNs) in the following.

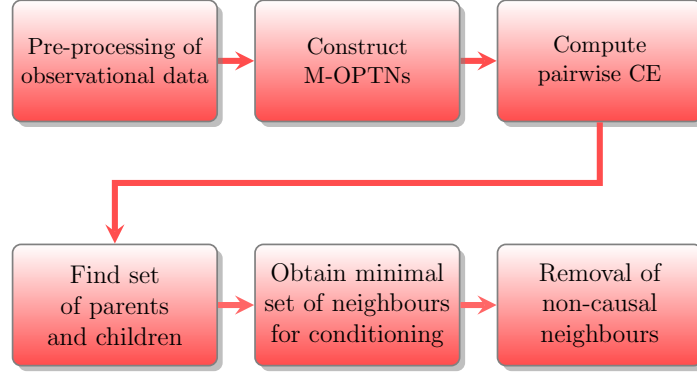


Figure 3: Proposed methodology

Algorithm 1 Construct M-OPTN from multivariate time series

```

1: procedure COMPUTEM-OPTN
2:   Input: Multivariate time series  $X_1, X_2, \dots, X_N$ , embedding dimension  $M$ , and lag  $d$ .
3:   Output: M-OPTN  $\Pi$ 
4:   for  $n = 1$  to  $N$  do
5:     for  $t = 1$  to  $T - (M - 1)d + 1$  do
6:       Map  $\mathbf{z}_{n,t}$  to symbol  $(s_0, \dots, s_{M-1})$  using Equations (2) to (3).
7:       Assign ordinal patterns  $\Pi[t, n] = \pi_k^{X_n}$  based on the respective permutation for each  $t$  and  $n$ .
8:     end for
9:   end for
10: end procedure

```

STEP III : Conditional entropy from M-OPTN

After constructing the M-OPTN, we compute the bivariate information theoretic measure of conditional entropy (CE) as given in Equation (5) for each pair of variables define the following matrix,

$$\mathbf{H}_\tau = \begin{bmatrix} H_\tau(X_1) & H_\tau(X_1|X_2) & \cdots & H_\tau(X_1|X_N) \\ H_\tau(X_2|X_1) & H_\tau(X_2) & \cdots & H_\tau(X_2|X_N) \\ \vdots & \vdots & \ddots & \vdots \\ H_\tau(X_N|X_1) & H_\tau(X_N|X_2) & \cdots & H_\tau(X_N) \end{bmatrix} \quad (7)$$

where each off-diagonal term $H_\tau(X_n|X_m)$ represents a possible causal link from the $m - th$ time series to the $n - th$ time series, i.e., $X_m \rightarrow X_n$, at delay τ . Note that in what follows, we will not make use of the diagonal elements of \mathbf{H}_τ (representing the classical Shannon entropies – i.e. in our specific case the permutation entropies – of the individual processes), so that they could be safely ignored or just put to zero.

Let $\mathbf{H} = \{\mathbf{H}_{\tau_1}, \mathbf{H}_{\tau_2}, \dots, \mathbf{H}_{\tau_J}\}$ denote the CE matrices obtained from the M-OPTN for a range of J delays $\mathbf{T} = \{\tau_1, \dots, \tau_J\}$. Each of the matrices \mathbf{H}_τ obtained above is next thresholded using a hard threshold to obtain a new matrix $\hat{\mathbf{H}}_\tau$ with elements

$$\hat{H}_\tau(X_n|X_m) = h_{nm\tau} = \begin{cases} H_{max}, & \text{if } H_\tau(X_n|X_m) \geq \lambda H_{max} \\ H_\tau(X_n|X_m), & \text{otherwise} \end{cases} \quad (8)$$

where $H_{max} = \log_2 M!$ and λ is usually set between 0.95 and 1. Due to the finite sample size, two independent processes will not have a CE value exactly equal to H_{max} . To account for this numerical issue, we allow for some tolerance by setting the parameter λ . After this step, only dominant neighbours (both causal and non-causal) are retained for each node. The matrix $\hat{\mathbf{H}}_\tau$ represents a weighted, directed network of N nodes, where the strength of the link between the node at delay τ is inversely proportional to the CE value $H_\tau(X_n|X_m)$ and no link exists between two nodes if $H_\tau(X_n|X_m) < \lambda H_{max}$.

Algorithm 2 Compute pairwise CE using M-OPTN

```

1: procedure COMPUTECE
2:   Input: M-OPTN  $\Pi$ , threshold  $\lambda$  and range of delays  $\mathbf{T} = \{\tau_1, \dots, \tau_J\}$ .
3:   Output: CE matrix  $\hat{\mathbf{H}}$ 
4:   for  $i = 1$  to  $J$  do
5:     for  $n = 1$  to  $N$  do
6:       for  $m = 1$  to  $N$  do
7:         Compute  $H_{\tau_i}(X_n|X_m)$  using Equation (5)
8:       end for
9:     end for
10:  end for
11:  Set  $\mathbf{H} = [\mathbf{H}_{\tau_1}, \mathbf{H}_{\tau_2}, \dots, \mathbf{H}_{\tau_J}]$ .
12:  Threshold  $\mathbf{H}$  using  $\lambda$  and  $H_{max}$  as shown in Equation (8).
13: end procedure

```

STEP IV : Find set of parents and children

The set of matrices $\hat{\mathbf{H}} = \{\hat{\mathbf{H}}_{\tau_1}, \hat{\mathbf{H}}_{\tau_2}, \dots, \hat{\mathbf{H}}_{\tau_J}\}$ represents a weighted multi-layer network $G = \{V, E\}$, where $V = \{X_1, \dots, X_N\}$ denotes a set of nodes (i.e. the different component processes) common to the different layers (which represent the different delays τ_j), while $E = \{E_1, \dots, E_J\}$ is a set of edges that will commonly differ among the layers. For every node X_m in the multi-layer network defined by $\hat{\mathbf{H}}$, we identify a set of k_m parents $\mathcal{P}_{X_m} = \{p_1, \dots, p_k\}$ at delays $\{\tau_{p_1}, \dots, \tau_{p_k}\}$ and l_m children $\mathcal{C}_{X_m} = \{c_1, \dots, c_l\}$ at delays $\{\tau_{c_1}, \dots, \tau_{c_l}\}$, respectively, which can span across all possible layers. The set of parents for a node X_m is given by

$$\mathcal{P}_{X_m} = \{h_{mn\tau} | h_{mj\tau} < H_{max}, n \neq m, \tau \in \mathbf{T}\} \quad (9)$$

where $h_{mj\tau}$ describes the element in row m and column j of the single-layer adjacency matrix $\hat{\mathbf{H}}_{\tau}$, cf. Equation (8). In a completely analogous way, we define the set of children of X_n node as

$$\mathcal{C}_{X_n} = \{h_{mn\tau} | h_{in\tau} < H_{max}, m \neq n, \tau \in \mathbf{T}\} \quad (10)$$

where $h_{in\tau}$ represents the element in row i and column n of $\hat{\mathbf{H}}_{\tau}$. By defining those two sets for all nodes (variables) X_m (X_n), we collapse the information contained in the multi-layer adjacency matrix $\hat{\mathbf{H}}$ to the essential strong bivariate (time-lagged) linkages among the set of considered variables.

Algorithm 3 Find set of parents and children from pairwise CE matrix

```

1: procedure FINDPC
2:   Input: Set of matrices  $\mathbf{H}$ ,  $H_{max}$ .
3:   Output:  $\mathcal{P}_{X_n}$  at delays  $\{\tau_{p_1}, \dots, \tau_{p_k}\}$  and  $\mathcal{C}_{X_n}$  at delays  $\{\tau_{c_1}, \dots, \tau_{c_l}\}$  for each node  $X_n$ .
4:   for  $n = 1$  to  $N$  do
5:     Compute  $\mathcal{P}_{X_n}$  and  $\mathcal{C}_{X_n}$  using Equation (9) and (10).
6:   end for
7: end procedure

```

STEP V : Identifying the minimal set of neighbours for conditioning

Given a set of parents for node X_m , $\mathcal{P}_{X_m} = \{p_1, \dots, p_k\}$ at delays $\{\tau_{p_1}, \dots, \tau_{p_k}\}$, to test for a causal connection from node X_n to node X_m , we seek to define a minimal conditioning set $\mathcal{P}_{X_m}^{min} \subset \mathcal{P}_{X_m}$, given as

$$\mathcal{P}_{X_m}^{min} = \mathcal{P}_{X_m} \cap \hat{\mathcal{C}}_{X_n} = \{p'_1, \dots, p'_r\} \quad (11)$$

where $\hat{\mathcal{C}}_{X_n}$ is the set of children of node X_n , which does not include X_m , i.e. $\hat{\mathcal{C}}_{X_n} = \mathcal{C}_{X_n} \setminus X_m$. The set $\hat{\mathcal{C}}_{X_n}$ will be an empty set if $\mathcal{C}_{X_n} = \{X_m\}$, i.e. the only child of node X_n is node X_m , and in this case we set $\mathcal{P}_{X_m}^{min} = \{X_m\}$. Also, it is possible that $\mathcal{P}_{X_m}^{min}$ will be an empty set due to no common elements between \mathcal{P}_{X_m} and $\hat{\mathcal{C}}_{X_n}$ and in this case we set $\mathcal{P}_{X_m}^{min} = \mathcal{P}_{X_m} \cap \mathcal{P}_{X_n}$. If $\mathcal{P}_{X_m}^{min}$ is still an empty set, then we set $\mathcal{P}_{X_m}^{min} = \{X_m\}$. Note that in each of these cases, along with the conditioning set $\mathcal{P}_{X_m}^{min}$, we also obtain the corresponding delays, $\{\tau'_1, \dots, \tau'_r\}$, with $|\mathcal{P}_{X_m}^{min}| = r$. In order to facilitate reliable computation of CE (see STEP VI) to exclude non-causal neighbours, in all our applications we restrict ourselves here to $r = 3$ if $r > 4$, by choosing the three most dominant neighbours, based on their respective CE values.

Algorithm 4 Find minimal set of neighbours for conditioning

```

1: procedure FINDMINCONDITIONINGSET
2:   Input:  $\mathcal{P}_{X_n}$  at delays  $\{\tau_{p_1}, \dots, \tau_{p_k}\}$  and  $\mathcal{C}_{X_n}$  at delays  $\{\tau_{c_1}, \dots, \tau_{c_l}\}$  for each node  $X_n$  and  $r$ .
3:   Output:  $\mathcal{P}_{X_m}^{min}$ 
4:   for  $m = 1$  to  $M$  do
5:     for  $n = 1$  to  $N$  do
6:       Set  $\hat{\mathcal{C}}_{X_n} = \mathcal{C}_{X_n} \setminus X_m$ 
7:       if  $\hat{\mathcal{C}}_{X_n} = \emptyset$  then
8:          $\mathcal{C}_{X_n} = \{X_m\}$ 
9:          $\mathcal{P}_{X_m}^{min} = \{X_m\}$ 
10:        break
11:      end if
12:      Set  $\mathcal{P}_{X_m}^{min}$  according to Equation (11).
13:      if  $\mathcal{P}_{X_m}^{min} = \emptyset$  then
14:         $\mathcal{P}_{X_m}^{min} = \mathcal{P}_{X_m} \cap \mathcal{P}_{X_n}$ 
15:      end if
16:      if  $\mathcal{P}_{X_m}^{min} = \emptyset$  then
17:         $\mathcal{P}_{X_m}^{min} = \{X_m\}$ 
18:      end if
19:    end for
20:  end for
21:  if  $|\mathcal{P}_{X_m}^{min}| > r$  then
22:    Set  $|\mathcal{P}_{X_m}^{min}| = r$ 
23:  end if
24: end procedure

```

STEP VI : Removal of non-causal neighbours by proper conditioning

To check if X_n is a truly causal parent to X_m , we compute

$$\epsilon_{X_n} = H(X_m | \mathcal{P}_{X_m}^{min}) - H(X_m | \mathcal{P}_{X_m}^{min}, X_n) \quad (12)$$

If X_n is an indirect causal connection to X_m , then $\epsilon_{X_n} = 0$, since conditioning on X_n should not reduce $H(X_m | \mathcal{P}_{X_m}^{min})$ any further. However, since we are dealing with finite data, $\epsilon_{X_n} \approx 0$. In practice, we set another pre-defined threshold δ and if $\epsilon_{X_n} < \delta$, then X_n is considered as an indirect causal link to X_m . The CE $H(X_m | \mathcal{P}_{X_m}^{min})$, with $|\mathcal{P}_{X_m}^{min}| = r$, is given as,

$$H(X_m | \mathcal{P}_{X_m}^{min}) = - \sum_{i=1}^{M!} \sum_{j=1}^{M!} p(\pi_i^{p'_1, \tau'_1}, \dots, \pi_i^{p'_r, \tau'_r}, \pi_j^{x_m}) \log p(\pi_j^{x_m} | \pi_i^{p'_1, \tau'_1}, \dots, \pi_i^{p'_r, \tau'_r}) \quad (13)$$

The conditional entropy $H(X_m | \mathcal{P}_{X_m}^{min}, X_n)$ is defined in an analogous way.

3 Numerical examples

In the following, we present results from the application of the proposed methodology to simulations of linearly interacting stochastic processes and interacting nonlinear dynamical systems using a network of neural mass models (NMMs).

For the simulations, we define the number of true positives (#TP) as the number of correctly identified links and number of false negatives (#FN) as number of missed links. The number of false positives (#FP) were defined as the number of incorrectly estimated links and the number of true negatives (#TN) were defined as number of correctly identified

Algorithm 5 Remove non-causal neighbours based on CE differences

```

1: procedure REMOVENCN
2:   Input: Matrix  $\mathbf{H}$ ,  $\delta$ .
3:   Output: Matrix  $\mathbf{H}$ .
4:   for  $m = 1$  to  $M$  do
5:     for  $n = 1$  to  $N$  do
6:       Compute  $\epsilon_{X_n}$  using Equations (12) and (13).
7:       if  $\epsilon_{X_n} < \delta$  then
8:         Set  $H(X_m|X_n) = H_{max}$ 
9:       end if
10:    end for
11:  end for
12: end procedure

```

non-links. We then define the true positive rate (TPR), false positive rate (FPR) and false discovery rate (FDR) as,

$$\begin{aligned}
TPR &= \frac{\#TP}{\#TP + \#FN} \\
FPR &= \frac{\#FP}{\#FP + \#TN} \\
FDR &= \frac{\#FP}{\#FP + \#TP}
\end{aligned} \tag{14}$$

3.1 Interacting stochastic processes

We simulated the following multivariate autoregressive (MVAR) system,

$$\begin{aligned}
x_{1,t} &= 3.4x_{1,t-1}(1 - x_{1,t-1}^2 e^{x_{1,t-1}^2}) + c_{21}x_{2,t-4} + c_{31}x_{3,t-2} + c_{41}x_{4,t-2} + 0.4u_{1,t} \\
x_{2,t} &= 3.4x_{2,t-1}(1 - x_{2,t-1}^2 e^{x_{2,t-1}^2}) + 0.4u_{2,t} \\
x_{3,t} &= 3.4x_{3,t-1}(1 - x_{3,t-1}^2 e^{x_{3,t-1}^2}) + c_{13}x_{1,t-1} + 0.4u_{3,t} \\
x_{4,t} &= 3.4x_{4,t-1}(1 - x_{4,t-1}^2 e^{x_{4,t-1}^2}) + c_{54}x_{5,t-3} + c_{64}x_{6,t-1} + 0.4u_{4,t} \\
x_{5,t} &= 3.4x_{5,t-1}(1 - x_{5,t-1}^2 e^{x_{5,t-1}^2}) + 0.4u_{5,t} \\
x_{6,t} &= 3.4x_{6,t-1}(1 - x_{6,t-1}^2 e^{x_{6,t-1}^2}) + c_{76}x_{7,t-3} + 0.4u_{6,t} \\
x_{7,t} &= 3.4x_{7,t-1}(1 - x_{7,t-1}^2 e^{x_{7,t-1}^2}) + 0.4u_{7,t} \\
x_{8,t} &= 3.4x_{8,t-1}(1 - x_{8,t-1}^2 e^{x_{8,t-1}^2}) + c_{78}x_{7,t-1} + 0.4u_{8,t} \\
x_{9,t} &= 3.4x_{9,t-1}(1 - x_{9,t-1}^2 e^{x_{9,t-1}^2}) + c_{79}x_{7,t-1} + 0.4u_{9,t}
\end{aligned} \tag{15}$$

with $c_{13} = 0.25$, $c_{21} = 2.5$, $c_{31} = 1.8$, $c_{41} = 1.5$, $c_{54} = 1.5$, $c_{64} = 1.2$, $c_{76} = 1.5$, $c_{79} = 1.8$, $c_{78} = 0.8$ and $u_{n,t}$ is zero mean Gaussian noise. The causal structure of the system described above is shown in Figure 4.

We vary the threshold δ from 0 to 0.2 in steps of 0.002, and for each value of threshold we generate 50 realizations for the system described in Equation (15). We varied the range of delays from 1 to 10 and the embedding dimension and delay was set to 3 and 100, respectively. We performed the simulations for data size of $T = 1000, 5000, 10000$ and 20000 samples.

Figure 5 shows the results from an exemplary simulation, where $\delta = 0.15$ and $N = 10000$ samples. As we can see from the figure, the causal interactions among the stochastic processes are correctly identified along with their respective delays. In Figure 5 the interaction $m \rightarrow n$ at a negative delay is to be interpreted as $n \rightarrow m$. The causal interaction between two processes at a particular delay results in a drop in the CE value from the H_{max} value, which in our case is given by, $\log M! \approx 2.58$.

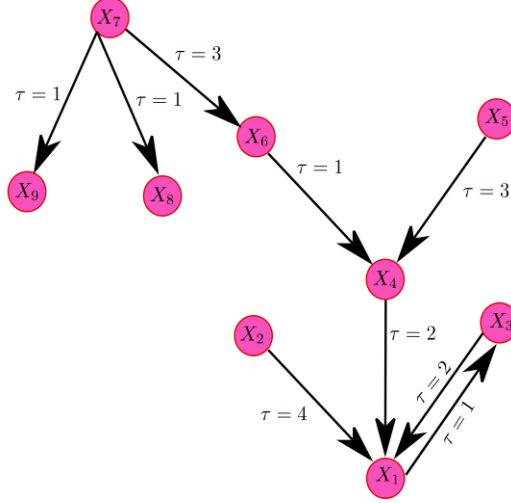


Figure 4: Multivariate autoregressive system (15).

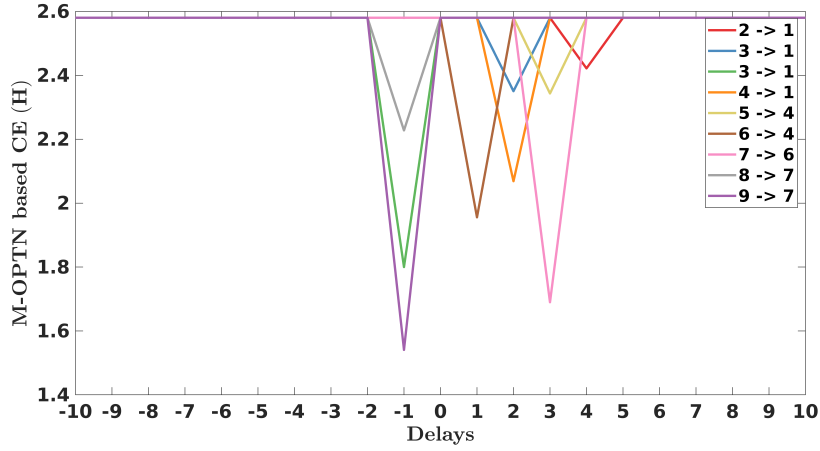


Figure 5: Causality detection based on M-OPTNs for an exemplary simulation of the MVAR system for $\delta = 0.15$ and $T = 10000$ samples.

Figure 6 shows the true positive rate (TPR) and false positive rate (FPR) respectively computed over 50 independent realizations of the MVAR system shown in Equation (15), for each δ as δ from 0 to 0.8 for $T = 1000, 5000, 10000$ and 20000 samples. Our results show that TPR is not affected by data length for $\delta < 0.2$ and starts to decrease as δ is increased, with the effect more prominent in cases where $T > 1000$. For $T = 1000$, we observe high FPR , which tends to decrease as δ is increased.

For $T \geq 5000$, FPR is below 0.05 and tends to zero as δ is increased. For $T \geq 10000$, FPR is zero for $\delta > 0.1$, whereas for $T = 5000$, $FPR = 0$ for $\delta > 0.15$.

Figure 7 shows the false discovery rate (FDR) as a function of δ , for various data length. As expected, for $T = 1000$, irrespective of the choice of δ , we have very high FDR values. For $\delta < 0.15$, we can see that FDR becomes zero for $T = 5000$ and $T = 10000$ and in case of $T = 20000$, for $\delta > 0.2$, we FDR mostly remains zero.

3.2 Network of neural mass models

The simulation described in Section 3.1 has been restricted to linear stochastic systems and may not fully characterize the nonlinearity present in neuronal oscillations. In order to also demonstrate the ability of the proposed method to capture interactions in nonlinear dynamical systems such as neuronal networks, we use a network of neural mass models (NMMs) [23]. To this end, we created a network of eight NMMs (the ordinary differential equations describing

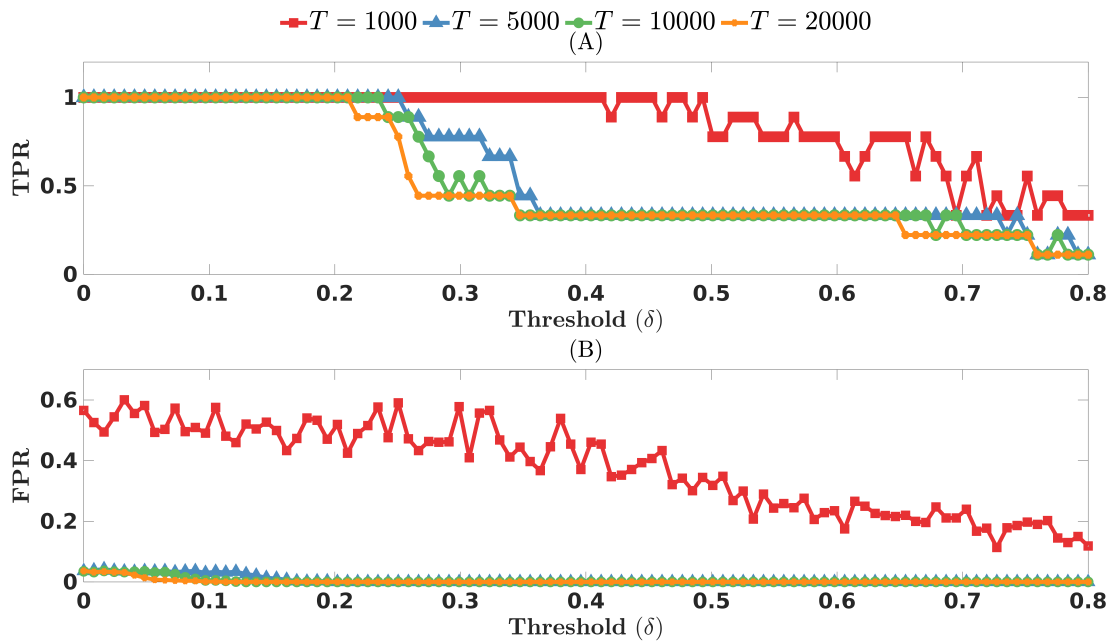


Figure 6: TPR (A) and FPR (B) computed for 50 independent realizations of the MVAR system as δ is varied from 0 to 0.8.

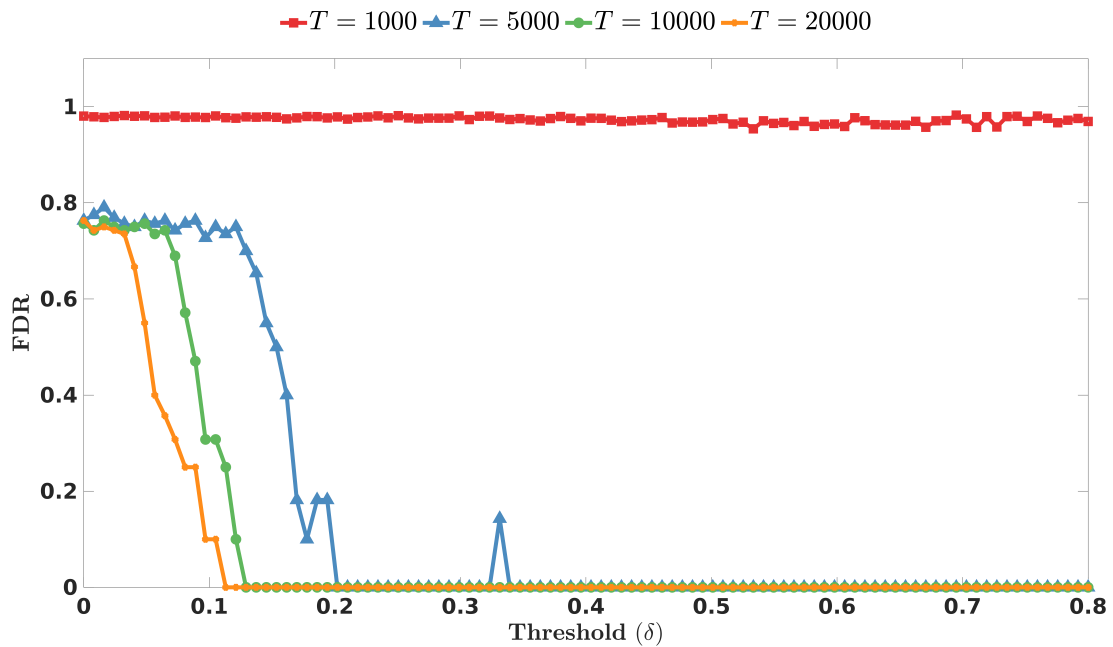


Figure 7: FDR computed for 50 independent realizations of the MVAR system as δ is varied from 0 to 0.8.

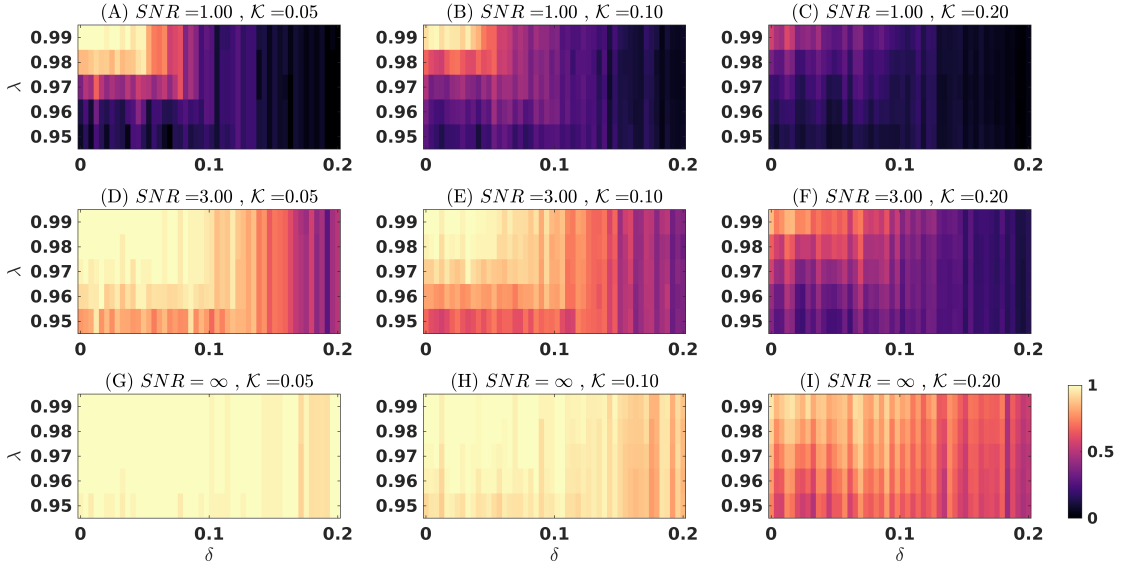


Figure 8: TPR computed for 50 independent realizations of network of NMMs for every combination of \mathcal{K} , λ , δ , and SNR.

each neural mass model is shown in the appendix and the parameters are set as given in [23]), with the % of directed interactions (\mathcal{K}) between the eight regions varying as 5%, 10% and 20% of the overall possible connections (N^2 including N self-connections), at a delay of 40 milliseconds. We varied the threshold λ from 0.95 to 0.99 and the threshold δ from 0 to 0.2. To also investigate the effect of noise on the performance of the method, in addition to the noise free observations from NMMs, Gaussian noise at two signal-to-noise ratios (SNRs) of 1.0 and 3.0 was added to the output of the NMMs. For each of the combination of these parameters (\mathcal{K} , λ , δ , and SNR) we generated 20 simulations. The embedding parameters were the same as in Section 3.1 ($M = 3$ and $d = 100$). We computed CE based on M-OPTNs for delays ranging from 10 milliseconds to 100 milliseconds. Since the interaction in the simulated network happens at around 40 milliseconds, any interaction in the estimated networks at a delay other than 40 milliseconds is counted as a false positive.

Figure 8 shows the TPR for the network of neural mass models for varying SNR, λ , δ and \mathcal{K} . We can see that for $\mathcal{K} = 0.05$ and $\mathcal{K} = 0.1$, TPR is largely unaffected by the choice of δ and λ for the noise free scenario (SNR = ∞), although highest TPR values (≈ 1) are observed for $\lambda = 0.99$ and $\delta < 0.1$. At SNR = 3.0, $\delta > 0.1$ causes the TPR to decrease and worst performance in terms of TPR is obtained for $\lambda = 0.95$. For $\lambda > 0.97$ and $\delta < 0.08$, high values for TPR are found. In case of SNR = 1.0, setting $\lambda = 0.99$ $\delta < 0.05$ gives TPR close to 1, with TPR decreasing for higher δ or lower λ .

When the connection density, \mathcal{K} is increased to 0.20, we observe that the scenario of SNR = ∞ performs the best, with the addition of noise decreasing the TPR. In particular, with $\lambda < 0.99$, we observe that for SNR = 3.0, the TPR mostly remains below 0.5, irrespective of the choice of the threshold δ . With $\lambda = 0.99$, for $\delta < 0.05$, TPR is around 0.8. For SNR = 1.0, $\lambda < 0.99$, irrespective of the choice of δ , the TPR remains below 0.25. When λ is increased to 0.99, TPR increases to 0.5 for $\delta < 0.03$ and then starts to decrease rapidly.

When looking at the results for the FPR for network of NMMs from Figure 9, we observe that irrespective of the SNR, λ or δ , for $\mathcal{K} = 0.05$ and $\mathcal{K} = 0.1$, the FPR remains below 0.1. When $\mathcal{K} = 0.20$, SNR = ∞ gives the highest FPR of around 0.2 for $\delta < 0.1$ and $\lambda = 0.99$. For lower λ , the FPR remains below 0.1 for all δ . In case of $\mathcal{K} = 0.2$, with SNR = 1.0 and SNR = 3.0, FPR again remains below 0.1 for all δ and λ .

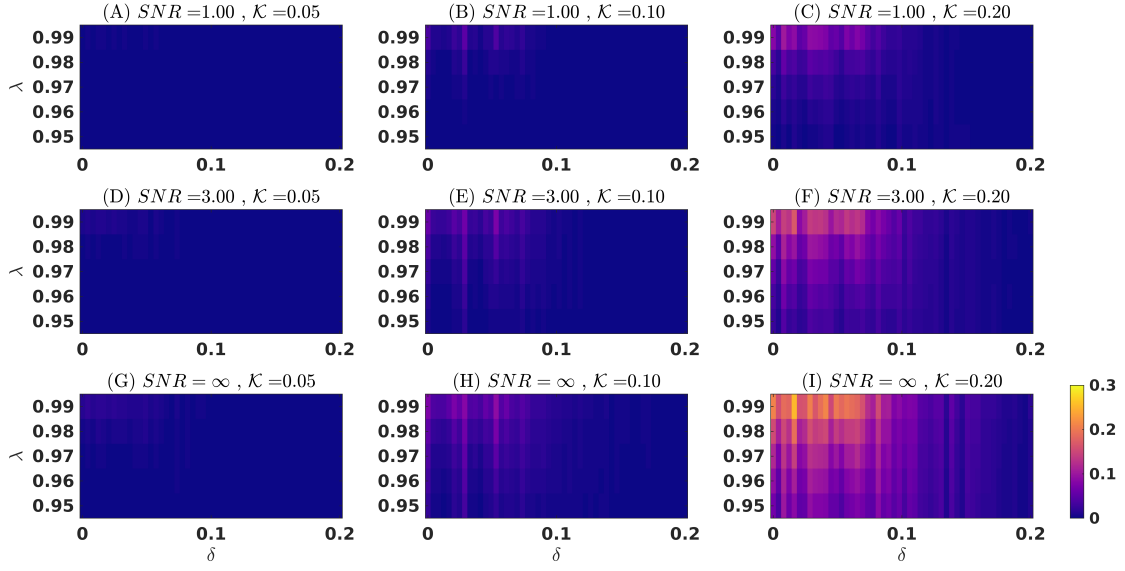


Figure 9: FPR computed for 50 independent realizations of network of NMMs for every combination of \mathcal{K} , λ , δ , and SNR.

4 Causality detection in MEA data

4.1 MEA data description

4.1.1 Brain slice preparation and maintenance

Combined hippocampus-cortex (CTX) brain slices, $400 \mu\text{m}$ thick, were prepared from male CD1 mice 4-8 weeks old. Animals were decapitated under deep isoflurane anesthesia, their brain was quickly removed and placed into ice-cold ($\approx 2^\circ\text{C}$) sucrose-based artificial cerebrospinal fluid (sucrose-ACSF) composed of (mM): Sucrose 208, KCl_2 , KH_2PO_4 1.25, MgCl_2 5, MgSO_4 , CaCl_2 0.5, D-glucose 10, NaHCO_3 26, L-Ascorbic Acid 1, Pyruvic Acid 3. The brain was let chill for 2 min before slicing in ice-cold sucrose-ACSF using a vibratome (Leica VT1000S, Leica, Germany). Brain slices were immediately transferred to a submerged holding chamber containing room-temperature holding ACSF composed of (mM): NaCl 115, KCl_2 , KH_2PO_4 , 1.25, MgSO_4 1.3, CaCl_2 2, D-glucose 25, NaHCO_3 26, L-Ascorbic Acid 1. After at least 60 minutes recovery, individual slices were transferred to a submerged incubating chamber containing warm ($\approx 32^\circ\text{C}$) holding ACSF for 20-30 minutes and subsequently incubated in warm ACSF containing the K^+ channel blocker 4-aminopyridine (4AP, $250 \mu\text{M}$), in which MgSO_4 concentration was lowered to 1 mM (4AP-ACSF, [24]). Brain slice treatment with 4AP is known to enhance both excitatory and inhibitory neurotransmission and induce the acute generation of epileptiform discharges [25]. All brain slices were incubated in 4AP-ACSF for at least 1 hour before beginning any recording session. All solutions were constantly equilibrated at $\text{pH} \approx 7.35$ with 95% O_2 / 5% CO_2 gas mixture (carbogen) and had an osmolality of 300-305 mOsm/kg. Chemicals were acquired from Sigma-Aldrich. All procedures been approved by the Institutional Animal Welfare Body and by the Italian Ministry of Health (authorization 176AA.NTN9), in accordance with the National Legislation (D.Lgs. 26/2014) and the European Directive 2010/63/EU. All efforts were made to minimize the number of animals used and their suffering.

4.1.2 Microelectrode array recording

Individual brain slices were placed on a 6×10 planar MEA (Ti-iR electrodes, diameter $30 \mu\text{m}$, inter-electrode distance $500 \mu\text{m}$, impedance $< 100 \text{k}\Omega$), held in place by a custom anchor, and continuously perfused at $\approx 1 \text{ml/min}$ with 4AP-ACSF at ($\approx 32^\circ\text{C}$), equilibrated with carbogen. Extracellular field potentials were acquired at 5 kHz (pre-sampling low-pass filter at 2 kHz) using the MEA2100-mini-HS60 system through the Multichannel Experimenter software (all from Multichannel Systems – MCS, Reutlingen, Germany). To allow for laminar flow and a high exchange rate of the 4AP-ACSF, a custom-made low-volume ($\approx 500 \mu\text{l}$) recording chamber (Crisel Instruments, Italy) replaced the default MEA ring [24].

4.1.3 Signal pre-processing

Observational electrophysiological data from rodent brain slices has been pre-processed which include standard procedures of low-pass filtering (1000 Hz), resampling (5000 to 3000 Hz). The data is then further divided into a number of overlapping windows (≈ 4 seconds) to obtain time-varying measure of causality.

4.1.4 Epileptiform activity generated by brain slices

To validate our approach against real-world experimental data, we applied the developed algorithm to electrophysiological recordings of epileptiform patterns generated by rodent hippocampus-cortex (CTX) slices treated with 4-aminopyridine (4AP). This brain slice preparation includes the fundamental circuits involved in the generation of limbic seizures seen in temporal lobe epilepsy (TLE) and enables analyzing the network interactions leading to seizure-like discharge generation. As shown in Figure 10, the key regions of interest (ROIs) in this brain slice preparation are the dentate gyrus (DG), the hippocampal subfields Cornu Ammonis 3 and 1 (CA3 and CA1, respectively), the subiculum (SUB) and the parahippocampal cortex (CTX). These regions communicate through the so-called hippocampal loop [26] (see Figure 10 (A)). When challenged with convulsant drugs, such as 4AP, hippocampus-CTX slices generate a typical complex epileptiform pattern made of three types of activity [27]: (i) slow interictal events, recurring at 5-20 s interval, generated by and spreading to any ROI with no specific site of origin, (ii) fast interictal events, recurring at 0.5-2 s interval, generated specifically by the CA3, propagating to the CA1 via the Schaffer Collaterals and subsequently reaching the CTX through the SUB (output gate), (iii) ictal (seizure-like) discharges, recurring at 3-5 min interval, originating primarily in the CTX and spreading to the hippocampus proper via the DG (input filter). It has been previously demonstrated that when the hippocampal loop circuitry is intact (connected brain slice), the fast CA3-driven interictal activity controls ictal discharge generation by the CTX, for which ictal discharges disappear over time, within 1-2 hours of 4AP application, while only the interictal patterns remain. At variance, the disruption of the hippocampal loop upon Schaffer Collaterals damage, as seen in hippocampal sclerosis typical of TLE (disconnected brain slice) releases the CTX from the CA3 control and allows ictal activity to originate and spread again [28].

Here, we have analyzed MEA recordings of epileptiform activity generated by disconnected hippocampus-CTX brain slices. in which disruption of the hippocampal loop was attained by mechanically severing the Schaffer Collaterals.

The circuit diagram of a disconnected hippocampus-CTX slice is depicted in Figure 10 (A) and Figure 10 (B) shows a disconnected hippocampus-CTX slice placed on a MEA. Figure 10 (C) shows the typical epileptiform pattern induced by 4AP in this brain slice preparation.

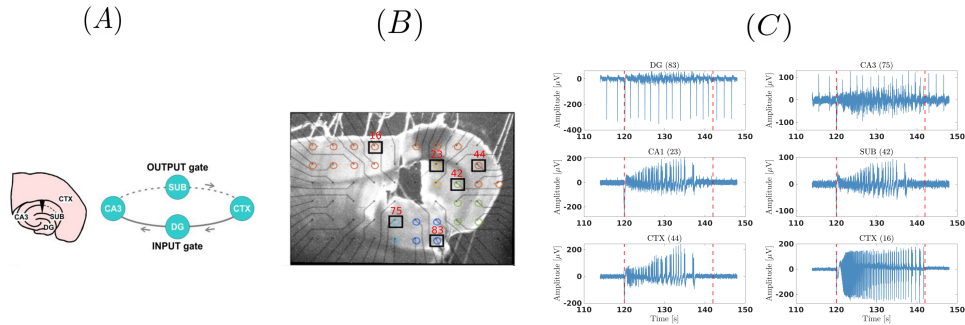


Figure 10: (A) Diagram of a disconnected hippocampus-CTX slice and its corresponding circuit. (B) Hippocampus-CTX slice with MEA electrodes placed in DG (blue), SUB (green), CA1 (yellow), CA3 (cyan) and CTX (orange). (C) MEA recording ranging from 114 seconds to 148 seconds from six selected electrodes, boxed in black and numbered in red in A. The onset and end of the ictal event occur at ≈ 120 and ≈ 142 s, respectively, as marked by the dashed red vertical lines.

For the purpose of the study we selected six electrodes (marked by the black rectangles in Figure 10 (B)), one in each of the four hippocampal regions and two electrodes from the CTX. MEA signals were low pass filtered to 1000 Hz and resampled to 3000 Hz from the original sampling frequency of 5000 Hz. CE based on M-OPTN was computed for each window and the resulting network was assigned to the mid point of each window.

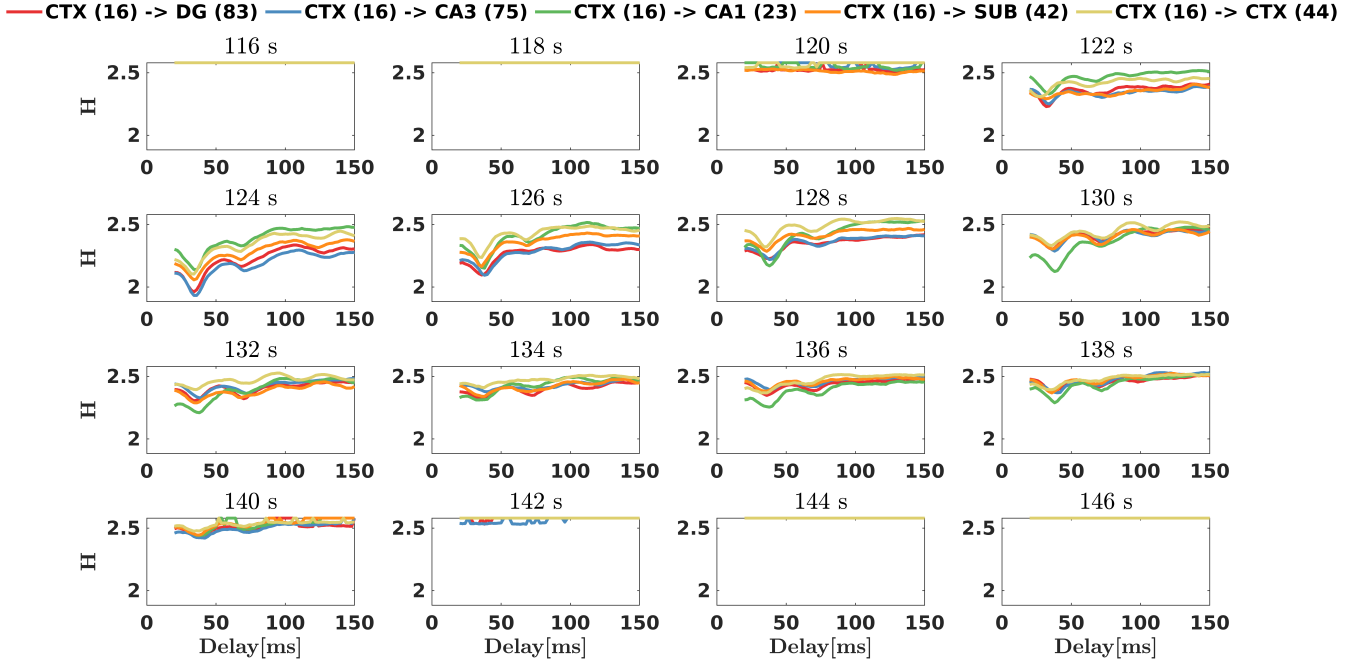


Figure 11: Causality detection based on M-OPTNs for MEA data. Each subplot represents outward connection from the CTX(16) to the other ROIs. The time window moves from 4 seconds before the ictal event to 4 seconds after it.

4.2 Results

The results from the application of our method are shown in Figure 11. We used a moving window of length 4 seconds, with 50% overlap starting at 114 s and ending at 148 s with entropy value assigned to the mid-point of the windows. The result shows the outward connections from an electrode in the CTX (electrode number 16) to all other ROIs, where the interaction is tested for delays ranging from 20 ms to 150 ms. The network activity starts around the time of the ictal event, with the strongest connections following the propagation paths CTX (16) \rightarrow DG (83) and CTX (16) \rightarrow CA3(75), occurring at around 122 seconds. The delay of this interaction is approximately 35 milliseconds. The strength of this outward connection further increases at 124 seconds, with outward connections from CTX (16) to all other regions, again with the strongest connections to DG (83) and CA3 (75). At around 128 seconds, the connection path CTX (16) \rightarrow CA1 (23) emerges as the strongest connection with a delay of around 38 milliseconds and this connection is retained until the end of the ictal event. Throughout the ictal event, the connection paths CTX (16) \rightarrow CTX (44) and CTX (16) \rightarrow SUB (42) are comparatively weaker than the CTX connections to the other ROIs. Figure 12 shows the conditional entropy values zoomed between the delays 20 and 50 ms for better representation of the results. Overall, these results are consistent with the anatomical and functional circuitries described within this brain slice preparation [26, 27], supporting the applicability and robustness of our method.

5 Discussion and Conclusions

In this work, we have proposed a new method to detect causality from multivariate observational data by computing information theoretic measures such as conditional entropy (CE) upon the resulting multiple ordinal partition transition networks (M-OPTNs). For reliable computation of CE and removal of non-causal neighbours, we have also proposed a pragmatic methodology to define a minimal set for conditioning variables. Our numerical experiments show that our approach can be used to reliably infer both the directionality and the delay of the interactions between the signals even at low and moderate signal-to-noise ratio (SNR). Causal network inference from real world data such as microelectrode array (MEA) recordings demonstrates that the application of the proposed method gives physiologically plausible results.

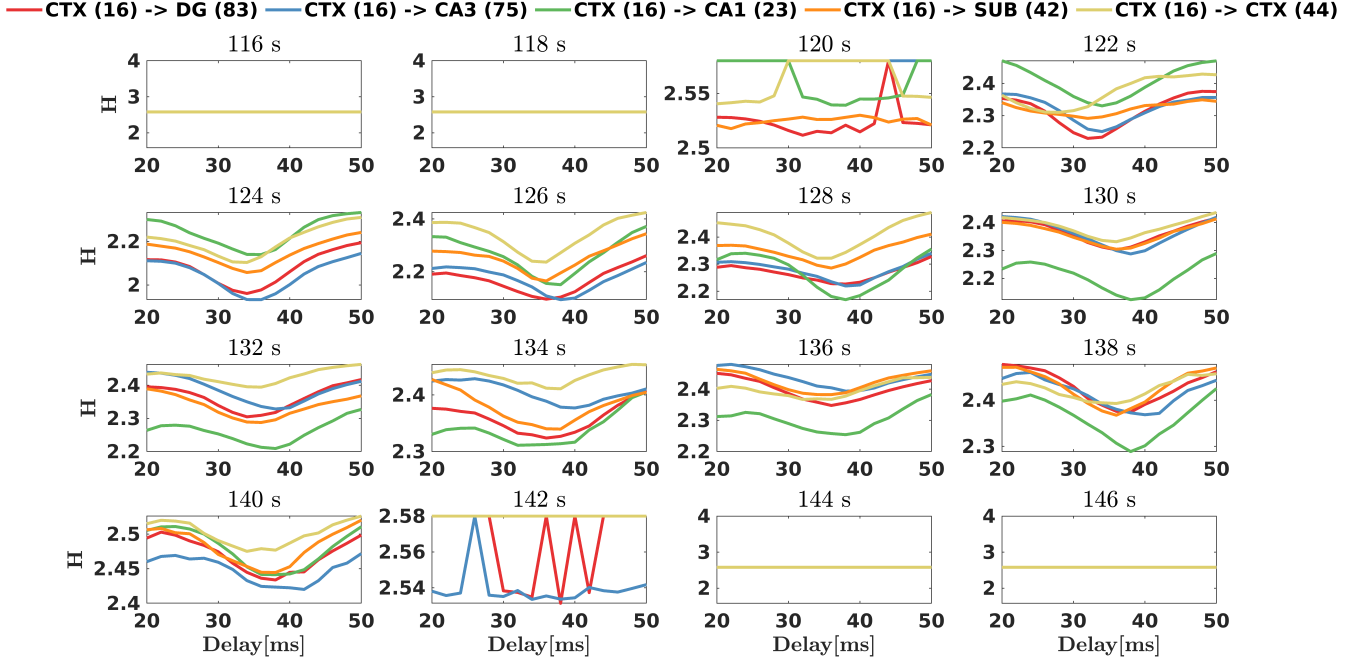


Figure 12: Causality detection based on Multipartite OPTNs for MEA data. Each subplot represents the outward connection from the CTX(16) to the other ROIs. The time window moves from 4 seconds before the ictal event to 4 seconds after it.

5.1 Minimal set of neighbours for conditioning

In order to test if a node (signal) m has a causal influence on node (signal) n , the standard and most common approach is to use the Peter and Clarke (PC) algorithm [29], that tests the conditional independence between these two nodes given all other variables. Non-existence of a causal relationship between m and n is established once it finds that m and n are conditionally independent given other variables. When inferring causality on multivariate time series, the conditioning set could have many such variables resulting in very unreliable estimates of information theoretic measures due to limited sample size. We alleviate this problem by defining a selection of variables to condition on, based on the common information shared between them. Furthermore, we restricted the number of variables to condition on, r to be no more than 3 as given the finite data size ($T \approx 10000$ samples), conditioning on a higher number of variables resulted in unreliable estimates of CE. In addition to the PC algorithm, there are other iterative, constraint-based approaches have been proposed to for conditioning, including the modified PC algorithm [29] and fast causal inference (FCI) algorithm [30] as well as score-based algorithm such as Greedy Equivalence Search (GES) [31] for defining conditioning sets. However, most of these algorithms have undesirable computational complexity and are not straightforward to implement. A systematic comparison of various conditioning approaches is beyond the scope of this work, where the motivation is to propose and demonstrate a extension to OPTN to infer causality in a reliable manner.

5.2 Effect of various parameters

Our numerical results from simulations of coupled stochastic processes, involving connections at different delays, have shown that the proposed approach can successfully capture the coupling directions and their delays. When applied on more realistic simulations using a network of neural mass models (NMMs) with 8 nodes and varying connection density, our approach could reliably recover the underlying causal coupling structure. However, the performance of the proposed method depends on the choice of several parameters as discussed in detail in the following sections.

5.2.1 Effect of varying the number of time samples

It is well known that the amount of data required for reliable reconstruction of the attractor depends on the embedding dimension M . Since the probability distributions required for the computation of CE are estimated from the ordinal

patterns obtained after embedding, inadequate data length might result in unreliable estimates of CE. In our simulations we have set $M = 3$ and found that the results are reliable if $T \gtrsim 10^3$. For a given M , there are $(M!)^2$ possible pairs of ordinal patterns for which we have to estimate the co-occurrence frequencies. Having $T \leq 10^M$ results in many spurious interactions being classified as causal links, which is reflected as an increase in the FPR as shown in our simulations. For both the stochastic model system and the network of NMMs, we used $M = 3$. Embedding in a higher dimension, for example $M = 5$ would require $T > 100000$ samples for reliable embedding and computation of entropy values. The typical sampling frequency of real-world data such as MEA recordings is of the order of 5000–10000 Hz, and to estimate dynamic changes in a causal effect network based on 100000 samples would mean using a window size of 10 to 20 seconds, which may be far too long compared to dynamical changes that occur in neural networks. Also, using 100000 samples or more, increases the computation time drastically. Thus, for electrophysiological recordings from neural data, a window size of 2 to 4 seconds seems more realistic, which amounts to having 10000 to 20000 samples per window, depending on the sampling frequency. This in turn means that the M should not be greater than 3 or at most 4. In contrast, we observed that varying the embedding delay did not affect the results qualitatively (not shown here) and we used $d = 100$ for all our simulations and real-world data.

5.2.2 Effect of varying threshold parameters to define significant connections

The parameter λ decides the significant connections (direct and indirect), with lower values pruning away most of the connections and higher values retaining most of the connections. When the network is less than 20% connected (edge density $\mathcal{K} < 0.2$, thereby involving $\sim \mathcal{KN}^2$ edges) and only a moderate amount of observation noise ($\text{SNR} > 1.0$ is present), we observe that $\lambda > 0.97$ seems to be the optimal setting that results in high TPR and low FPR based on our simulations of the NMM network, provided that δ is chosen optimally. The choice of δ , which determines the threshold to distinguish a causal neighbour from a non-causal neighbour, by computing the difference in the conditional entropy, depends on the amount of noise present in the data. In the presence of low or moderate observational noise, a truly causal neighbour would result in a high δ as conditioning on this neighbour should reduce the entropy significantly. In contrast, a non-causal neighbour would result in a very small δ . Our results show that setting $\delta \leq 0.1$ in such a scenario is an optimal choice along with $\lambda > 0.97$. If the data is very noisy ($\text{SNR} \leq 1$), then the necessary δ for identifying a truly causal neighbour would be very small, thereby making it hard to distinguish from a non-causal neighbour, for which δ should also be small. Thus setting δ too high will prune away all the true connections along with the spurious one, while setting δ too low might retain some spurious connections. For $\text{SNR} = 1$, we observe that $\delta < 0.05$ and $\lambda = 0.99$ can serve as an optimal setting.

Another factor that impacts the choice of λ and δ in addition to SNR is the number of connections in the network. When the network is more than 20% connected, finding an optimal δ and λ that gives high TPR and FPR is more challenging as the estimated network has many spurious connections at multiple delays in addition to the interaction at the correct delay. Any choice of δ to prune away these spurious connections also takes away the true connections as the SNR increases.

In summary, setting $\lambda = 0.99$ and varying δ between 0.05 and 0.1 should result in reliable network inference, assuming the underlying networks are sparse as shown by our simulations.

5.3 Causal network inference from MEA data

As a real-world example, we applied the proposed method to MEA electrophysiology recordings from rodent hippocampus-CTX slices treated with 4AP in which the Schaffer Collaterals were cut to mimick the hippocampal sclerosis disrupting the hippocampus-CTX loop in temporal lobe epilepsy patients. This surgical manipulation releases the CTX from the control exerted by the CA3 over ictal activity, thereby enabling seizure-like discharges to be generated by the CTX indefinitely. The MEA electrodes recorded epileptiform electrical activity from the DG, SUB, CA1 and CA3 as well as the CTX. In a previous study [28], the mean time delay for the ictal discharge propagation path $\text{CTX} \rightarrow \text{DG}$, $\text{CTX} \rightarrow \text{CA3}$ and $\text{CTX} \rightarrow \text{CA1}$ after severing the Schaffer Collaterals is 37.5 ± 9.6 ms, 71.7 ± 27.5 and 31 ± 6.3 ms. Consistent with these results, our method detects connectivity in the direction of $\text{CTX} \rightarrow \text{DG}$, $\text{CTX} \rightarrow \text{CA3}$ and $\text{CTX} \rightarrow \text{CA1}$ at delay of 30 to 38 milliseconds during the ictal discharge, suggesting that these measures can be useful for analyzing interactions and their delays among real world observations such as electrophysiological time series.

The present work demonstrates that combining concepts from symbolic time series analysis, transition networks and information theory can provide complementary tools for detecting causality. From a practical point of view, the proposed method is also data efficient, requiring a small number of samples (5000 to 10000 samples) to estimate causality, which is an important feature when inferring time-varying causal networks.

Acknowledgements

This project has received funding from the European Union's Horizon 2020 research and innovation programme FETPROACT-01-2018 (RIA) awarded to the project Hybrid Enhanced Regenerative Medicine Systems (HERMES) under grant agreement No 824164

Appendix: Equations for the neural mass model

The neuronal activity in one region is represented by the following differential equations:

Pyramidal neurons

$$\frac{dy_p(t)}{dt} = x_p(t), \quad (16)$$

$$\frac{x_p(t)}{dt} = G_e h_e z_p(t) - 2h_e x_p(t) - h_e^2 y_p(t) \quad (17)$$

$$z_p(t) = \frac{2e_0}{1 + e^{-rv_p}} - e_0 \quad (18)$$

$$v_p(t) = C_{pe} y_e(t) - C_{ps} y_s(t) - C_{pf} y_f(t) \quad (19)$$

Excitatory interneurons

$$\frac{dy_e(t)}{dt} = x_e(t), \quad (20)$$

$$\frac{x_e(t)}{dt} = G_e h_e \left(z_e(t) + \frac{u_p(t)}{C_{pe}} \right) - 2h_e x_e(t) - h_e^2 y_e(t) \quad (21)$$

$$z_e(t) = \frac{2e_0}{1 + e^{-rv_e}} - e_0 \quad (22)$$

$$v_e(t) = C_{ep} y_p(t) \quad (23)$$

Slow inhibitory interneurons

$$\frac{dy_s(t)}{dt} = x_s(t), \quad (24)$$

$$\frac{x_s(t)}{dt} = G_s h_s z_s(t) - 2h_s x_s(t) - h_s^2 y_s(t) \quad (25)$$

$$z_s(t) = \frac{2e_0}{1 + e^{-rv_s}} - e_0 \quad (26)$$

$$v_s(t) = C_{sp} y_p(t) \quad (27)$$

Fast inhibitory interneurons

$$\frac{dy_f(t)}{dt} = x_f(t), \quad (28)$$

$$\frac{x_f(t)}{dt} = G_f h_f z_f(t) - 2h_f x_f(t) - h_f^2 y_f(t), \quad (29)$$

$$\frac{dy_f(t)}{dt} = x_i(t), \quad (30)$$

$$\frac{x_i(t)}{dt} = G_e h_e u_f(t) - 2h_e x_i(t) - h_e^2 y_i(t), \quad (31)$$

$$z_f(t) = \frac{2e_0}{1 + e^{-rv_f}} - e_0 \quad (32)$$

$$v_f(t) = C_{fp} y_p(t) - C_{fs} y_s(t) - C_{fi} y_i(t) \quad (33)$$

References

- [1] J. Runge, Causal network reconstruction from time series: From theoretical assumptions to practical estimation, *Chaos*, 28, 075310 (2018)
- [2] K. Hlaváčková-Schindler, M. Paluš., M. Vejmelka, and J. Bhattacharya, Causality detection based on information-theoretic approaches in time series analysis. *Phys. Rep.*, 441, 1-46 (2007).
- [3] J. Sun and E.M. Bolt, Causation entropy identifies indirect influences, dominance of neighbors and anticipatory couplings. *Physica D*, 267, 49-57 (2014)
- [4] C.W.J. Granger, Investigating causal relations by econometric models and cross-spectral methods. *Econometrica*, 37, 424-438 (1969).
- [5] L.A. Baccala and K. Sameshima, Partial directed coherence: A new concept in neural structure determination. *Biol. Cybern.*, 84, 463-474 (2001).
- [6] A. Montalto, L. Faes and D. Marinazzo, MuTE: A MATLAB Toolbox to Compare Established and Novel Estimators of the Multivariate Transfer Entropy. *PLoS One*, 9, e109462 (2014).
- [7] T. Schreiber, Measuring information transfer. *Phys. Rev. Lett.*, 85, 461-464 (2000).
- [8] J. A. Vastano and H. L. Swinney, Information transport in spatiotemporal systems. *Phys. Rev. Lett.*, 60, 1773 (1988).
- [9] S. Li, Y. Xiao, D. Zhou, and D. Cai , Causal inference in nonlinear systems: Granger causality versus time-delayed mutual information. *Phys. Rev. E*, 97, 052216 (2018).
- [10] L. Barnett, A.B. Barrett, and A.K. Seth, Granger causality and transfer entropy are equivalent for Gaussian variables. *Phys. Rev. Lett.*, 103, 238701 (2009).
- [11] Y. Zou, R.V. Donner, N. Marwan, J.F. Donges and J. Kurths, Complex network approaches to nonlinear time series analysis. *Phys. Rep.*, 787, 1-97 (2019).
- [12] R.V. Donner, Y. Zou, J.F. Donges, N. Marwan and J. Kurths, Recurrence networks—a novel paradigm for nonlinear time series analysis. *New J. Phys.*, 12, 033025 (2010).
- [13] N. P. Subramaniyam and J. Hyttinen Characterization of dynamical systems under noise using recurrence networks: Application to simulated and EEG data. *Phys. Lett. A*, 378, 3464-3474 (2014).
- [14] N. P. Subramaniyam, J. F. Donges, and J. Hyttinen, Signatures of chaotic and stochastic dynamics uncovered with ϵ -recurrence networks. *Proc. R. Soc. A*, 471(2183), 20150349 (2015).
- [15] L. Lacasa, B. Luque, F. Ballesteros, J. Luque, and J. C. Nuno, From time series to complex networks: The visibility graph. *Proc. Natl. Acad. Sci. USA* 105(13), 4972 (2008).
- [16] M. McCullough, M. Small, T. Stemler and H.H.C. Iu, Time lagged ordinal partition networks for capturing dynamics of continuous dynamical systems. *Chaos*, 25, 053101 (2015).
- [17] Y. Ruan, R.V. Donner, S. Guan and Y. Zou, Ordinal partition transition network based complexity measures for inferring coupling direction and delay from time series. *Chaos*, 29, 043111 (2019).
- [18] M. McCullough M, K. Sakellariou , T. Stemler , M. Small, Counting forbidden patterns in irregularly sampled time series. I. The effects of under-sampling, random depletion, and timing jitter. *Chaos*, 26, 123103 (2016).
- [19] C. Bandt and B. Pompe, Permutation entropy: a natural complexity measure for time series. *Phys. Rev. Lett.*, 88, 174102 (2002).
- [20] J. Y. Zhang, J. Zhou, M. Tang, H. Guo, M. Small, and Y. Zou, Constructing ordinal partition transition networks from multivariate time series. *Sci. Rep.* 7, 7795 (2017).
- [21] C. W. Kulp, J. M. Chobot, H. R. Freitas, and G. D. Sprechini, Using ordinal partition transition networks to analyze ECG data. *Chaos*, 26, 073114 (2016).
- [22] K. Keller, A.M. Unakafov, and V.A. Unakafova, Ordinal patterns, entropy, and EEG. *Entropy*, 16, 6212-6239 (2014).
- [23] M. Zavaglia, F. Cona and M. Ursino, A Neural Mass Model to Simulate Different Rhythms in a Cortical Region. *Comput. Intell. Neurosci.*, 2010, 456140 (2010).
- [24] G. Panuccio, I. Colombi, and M. Chiappalone, Recording and Modulation of Epileptiform Activity in Rodent Brain Slices Coupled to Micro Electrode Arrays. *J. Vis. Exp.*, 135, e57548 (2018).
- [25] P. A. Rutecki, F. J. Lebeda, and D. Johnston, 4-Aminopyridine produces epileptiform activity in hippocampus and enhances synaptic excitation and inhibition. *J. Neurophysiol.*, 57, 1911-1924 (1987).

- [26] D. G. Amaral and M. P. Witter, The three-dimensional organization of the hippocampal formation: a review of anatomical data. *Neuroscience*, 31, 571-591 (1989).
- [27] M. Avoli, M. D'Antuono, J. Louvel, R. Köhling, G. Biagini, R. Pumain, G. D'Arcangelo, and V. Tancredi, Network and pharmacological mechanisms leading to epileptiform synchronization in the limbic system in vitro. *Prog. Neurobiol.*, 68, 167-207 (2002).
- [28] M. Barbarosie, J. Louvel, I. Kurcewicz and M. Avoli, CA3-released entorhinal seizures disclose dentate gyrus epileptogenicity and unmask a temporoammonic pathway. *J. Neurophysiol.*, 83, 1115-1124 (2000).
- [29] P. Spirtes, C.N. Glymour, R. Scheines, and D. Heckerman, *Causation, prediction, and search*. MIT Press, Boston (2000).
- [30] J. Ramsey, J. Zhang, and P. L. Spirtes, Adjacency-faithfulness and conservative causal inference. arXiv preprint [arXiv:1206.6843](https://arxiv.org/abs/1206.6843) (2012).
- [31] D. M. Chickering, Learning equivalence classes of Bayesian-network structures. *J. Machine Learn. Res.*, 2, 445-498 (2002).